

pubs.acs.org/acsaelm Article

Intriguing Two-Dimensional BeO-Based Tribo-Piezoelectric Nanogenerator

Md. Sherajul Islam,* Md. Yasir Zamil, Naim Ferdous, Catherine Stampfl, and Jeongwon Park



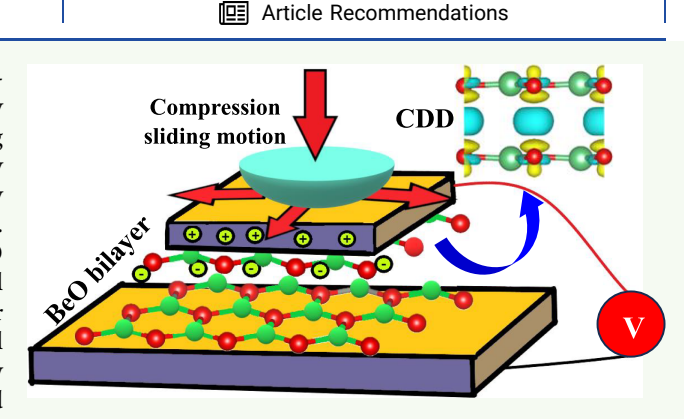
Cite This: ACS Appl. Electron. Mater. 2023, 5, 7034-7044



ACCESS I

Metrics & More

ABSTRACT: The remarkable piezoelectric characteristics manifested by two-dimensional (2D) materials render them immensely coveted candidates for deployment in nanoscale energy harvesting tools. In this study, we demonstrate the generation of nanoenergy from the tribo-piezoelectric effect in a 2D BeO bilayer system by employing first-principles density functional theory calculations. We find that compression and sliding motions between two BeO layers produce a substantial tribo-piezoelectric effect. Lateral sliding of the upper BeO layer while the bottom BeO layer remains fixed engenders tribological energy from the vertical resistance force. Through tribological energy conversion, we show how BeO bilayers may overcome the interfacial sliding barrier and generate tribo-piezoelectricity. We obtain maximum energy



corrugation in the range of 101-301 meV and shear strength in the range of 0.4-2.38 GPa during vertical compression. The highest out-of-plane piezoelectricity is obtained when the bilayers are in the A-A stacking configuration by lateral sliding. A maximum induced voltage of ~ 0.22 V is attained through the vertical compressive sliding of the upper layer. These findings offer potential opportunities for harvesting nanoenergy from the tribo-piezoelectric effect of BeO systems, paving the way for advancing the field of self-powered sensors, wireless electronics, and wearable devices.

KEYWORDS: nanoenergy, tribo-piezoelectric, 2D BeO, compression-sliding, polarization

INTRODUCTION

Energy harvesting technologies that can generate electricity from mechanical motion have received significant attention recently. 1-6 The piezoelectric effect is a widely used method to generate electrical energy from mechanical stress.^{2,4,7-10} The triboelectric effect, which involves the generation of charge separation due to friction between two materials, is another promising approach for energy harvesting. 11-18 In this context, nanogenerators based on tribo- and piezo-electric effects of materials have attracted increasing attention 19-21 due to their small size and scalability for various applications, such as selfpowered sensors,²² wireless electronics,^{23,24} and wearable devices. 25,26 However, tribo-piezoelectric nanogenerators (TPNGs) are still relatively inefficient compared to other energy harvesting techniques, such as solar cells²⁷ or thermoelectric²⁸ generators. Improving the efficiency of TPNGs is a major challenge and requires optimizing the materials and device design to maximize energy conversion.

The reduction of dimensionality can result in notable deviations in the material's properties from their bulk counterparts, often exhibiting unique or unexpected characteristics. ^{29–36} For example, two-dimensional (2D) graphene exhibits exceptional electrical and thermal conductivity as

well as extraordinary mechanical strength, doped 2D h-BN³⁷ demonstrates unusual optical and magnetic behaviors, and 2D metal dichalcogenides³⁸ show auspicious tunable band gap energies and catalytic edge effects. Piezoelectricity is another interesting and significant trait of 2D materials because it enables the transfer of energy between electrical and mechanical forms. Compared to bulk materials, 2D crystal structures exhibit a higher degree of anisotropy, which is characterized by a reduced number of symmetry elements.³⁹ The elimination of inversion symmetry in 2D structures is a common occurrence, leading to the emergence of piezoelectric properties in such materials. Compounds that display planar and buckled hexagonal structures can disrupt inversion symmetry and therefore demonstrate piezoelectric properties. 40 The exceptional piezoelectric properties exhibited by 2D materials make them a highly desirable candidate for utilization

Received: October 7, 2023
Revised: November 21, 2023
Accepted: November 22, 2023
Published: December 6, 2023





in the next generation of energy harvesting devices, transducers, sensors, and actuator applications. 33,41

In recent years, several 2D materials have been shown as promising candidates for the development of nanoscale energy harvesting devices. 41-43 Transition-metal dichalcogenides 2 (TMD) and Janus WSSe or WSTe monolayers have been found to display both vertical and in-plane piezoelectric properties. The generation of ferroelectricity due to sliding motion is reported for several bilayer structures of 2D materials. 44-51 Moreover, it has been demonstrated that group-III nitride bilayers display robust triboelectric and piezoelectric characteristics. 52 In this context, monolayer honeycomb beryllium oxide (BeO) has recently garnered significant interest in the realm of nanoscale device fabrication due to its unique properties, including a large electronic band gap (~6 eV),⁵³ exceptional mechanical strength, superior room temperature thermal conductivity (~270 W/m-K), 54,55 high excitonic binding energy,⁵⁶ and remarkable optical properties. 44 The anticipated substantial variation in electronegativity among the constituent elements, namely, Be (1.57) and O (3.44), seen in BeO is likely to lead to considerable polarization upon mechanical agitation. BeO offers excellent piezoelectric behavior (has the highest piezoelectric stress, e_{11} , coefficient among group II–IV oxide compounds 57), leading to the generation of electric charge in response to applied mechanical stress. Although 2D BeO is anticipated as a promising tribo-piezoelectric material for nano energy generation, a comprehensive understanding of the mechanisms underlying the piezoelectric and triboelectric phenomena involved in developing 2D BeO-based nanogenerators is currently lacking. Therefore, it is imperative to investigate the mechanism by which mechanical deformation and friction generate electrical potential prior to utilizing these materials for nanogenerator applications.

In this work, we explore the tribo-piezoelectric properties of 2D BeO through a comprehensive analysis utilizing ab initio density functional theory (DFT) calculations. Based on the investigated tribo- and piezoelectric responses, we propose a compression-sliding BeO nanogenerator. The shear strength, polarization deviation, and energy changes due to the changes in the in-plane sliding motion and the vertical distance between the two BeO layers have been calculated. Our findings indicate that the induction of vertical polarization in bilayer BeO can be achieved through transverse sliding along a specific direction of the BeO monolayers. During the transition to the A-A configuration with a fixed interlayer distance, there is a notable enhancement in the vertical polarization and no occurrence of triboelectric charges. The observation suggests that the generation of piezoelectricity has been induced through an increase in vertical polarization, 21 as opposed to the production of triboelectricity via tribological means.⁵⁸ It is noteworthy to state that tribo-piezoelectricity is distinct from traditional piezo-triboelectricity since triboelectric charges are never produced by interlayer sliding.

MODEL AND CALCULATION METHODS

We first considered a bilayer of BeO made of vertically stacking two BeO monolayers in order to explore the mechanical resistance and distortion. Bilayer BeO has a rhombic unit cell consisting of two beryllium (Be) and two oxygen (O) atoms. In order to attain the translation along the *xy* plane, the lower BeO layer was kept stationary while the upper BeO layer experienced transverse sliding. Accordingly, the system is translated to various points on the *xy* plane. Structural

optimization was performed in each translated point while a fixed vertical distance was maintained between the oxygen atoms of the upper and lower BeO layer. All through the in-plane horizontal moving of the top BeO layer on the xy plane with a constant interlayer spacing, the potential energy surface (PES) was quantified using the expression:

$$E_{\text{PES}}(x, y) = E(x, y) - E_{\min}$$
 (1)

With $E_{\rm PES}(x,y)$ signifying the PES at the xy coordinates. Herein, PES implies the potential energy of the structure due to the translation of the upper layer at various points across the xy plane while E(x,y) represents the energy achieved at a particular xy coordinate of the system, and $E_{\rm min}$ stands for minimum value of E(x,y) at which the total energy of the system is at its lowest. We obtained the comparative vertical polarization at a distinct xy coordinate $(P_{\rm D})$ through the relation:

$$P_{\rm D} = \frac{d}{A} \tag{2}$$

Here, d and A correspond to the dipole moment in the vertical direction and the area of the bilayer's unit cell. At the primary optimized state, charges are transferred to the oxygen atoms of the BeO sheets, attributable to the greater degree of electronegativeness of the oxygen atoms (3.44) compared to the beryllium atoms (1.57) which results in the out-of-plane polarization of the charges. Consequently, primary vertical polarization with zero (0) normal force $(P_{\rm FN})$ is taken as null. The polarization deviation surface²¹ (PDS) while performing the in-plane xy sliding was computed from the absolute value of the vertical polarization from the relation:

$$\delta P(x, y) = P_{\rm D}(x, y) - P_{\rm FN} \tag{3}$$

where $\delta P(x, y)$ is the PDS and $P_{\rm D}(x, y)$ stands for the vertical polarization at a distinct xy coordinate. A greater degree of the vertical dipole moment and polarization is expected, while the sliding resistance force between the two BeO sheets is accounted for. We determined the shear strength related to the in-plane xy translation of the upper layer as:

$$\tau = \left| \frac{F_{\text{MR}}}{A} \right| \tag{4}$$

where τ refers to the interlayer shear strength, which is attained from the highest static resistance force (F_{MR}) acting upon the BeO sheet with the area A during the lateral moving process of the upper layer.

For all the computations in this study, we utilized first-principles density functional theory (DFT) calculations as implemented in the plane wave self-consistent field (PWscf) Quantum Espresso^{59,60} suite. We used the Kresse-Joubert projected augmented wave⁶¹ (KJPAW) potentials to describe the interactions between the electrons and ions, while the Perdew–Burke–Ernzerhof⁶² generalized gradient approximation⁶¹ (PBE–GGA) was applied for the electron-correlation functional. The interaction between the two successive bilayers was avoided by introducing an adequate free space exceeding 20 Å along the z-axis. A Γ -centered 15 \times 15 \times 1 Monkhorst-Pack⁶³ grid was employed to sample the first Brillouin zone of the unit cell. To incorporate the van der Waals (vdW) intermolecular attractive forces, we used the optB86b-vdW⁶⁴ introduced by Klimeš et al. The optB86b-vdW is an improved version of the vdW-density functional 65 in which the original vdW density^{65,66} functional was substituted by the optB86b exchange functional to calculate more precise interatomic spacings and energies in equilibrium for a large variety of structures. The cutoff of the plane wave basis was taken as 50 Ry while the charge density cutoff was taken as 500 Ry. For the groundstate electron density to converge, we applied 10^{-7} au as the energy cutoff value. The convergence threshold on the force on the atoms was 10^{-3} Ry/au for calculating precise force and stress.

■ RESULTS AND DISCUSSION

The optimized structural parameters of free-standing singlelayered BeO were initially studied. Our calculation yielded 2.66

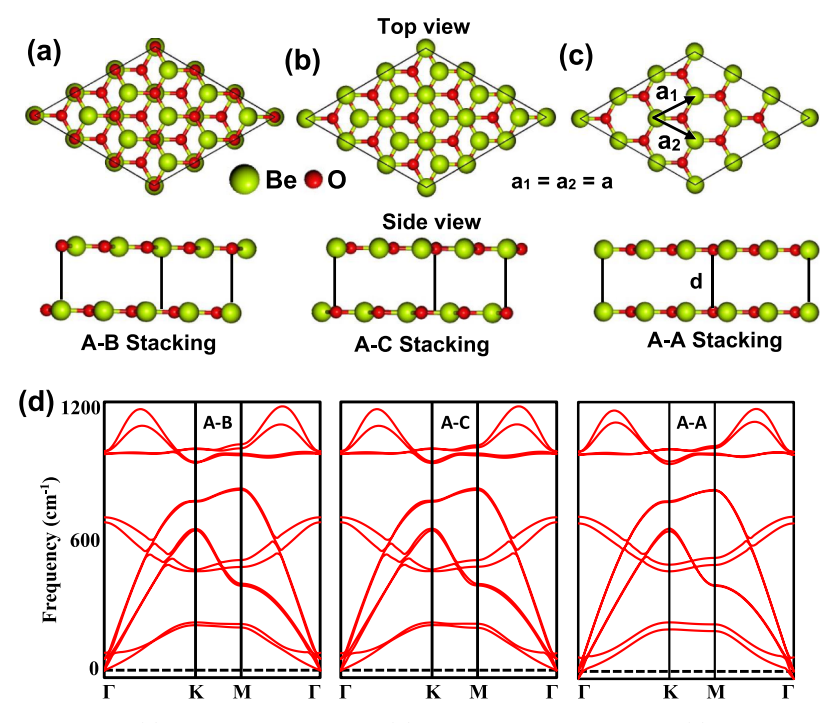


Figure 1. Bilayer structures of BeO with (a) A-B stacking pattern, (b) A-C stacking pattern, and (c) A-A stacking pattern. The green atoms represent the Be atoms, while the red atoms demonstrate the O atoms. The lattice parameter is represented by "a", and the interlayer distance is represented by "d". (d) Phonon dispersion relations for all the stacking configurations.

Å for the lattice constant along with a Be–O bond length of 1.535 Å, where the structure of the BeO single layer was fully relaxed. This is in close agreement with previous studies. 53,67 The BeO layer exhibits a planar honeycomb structure, similar to graphene, with no buckling present in the structure. The BeO bilayer was adapted by stacking two BeO layers vertically. Our study suggests that A–B and A–C were the two stable geometric configurations for the BeO bilayer, as confirmed by the absence of negative frequencies in the phonon dispersion relations (Figure 1d). As shown in Figure 1a, the A–B configuration has a bilayer structure with the O atom of the upper layer directly above the Be atom of the lower layer and the Be atom of the upper layer in the middle of the hexagon formed by the lower BeO sheet.

The A-C stacking geometry (Figure 1b) has the Be atoms of the top layer directly above the O atoms of the lower layer, while the O atoms of the upper layer are in the middle of the hexagon of the lower BeO sheet. The vertical distance between the O atoms of the upper and lower layers is taken as the interlayer spacing between the two monolayers. To obtain equilibrium interlayer spacing, the variation of the binding energy of the bilayer as a function of interlayer spacing is calculated. The A-B and A-C configurations yielded optimum interlayer distances of 3.03 and 3.04 Å, respectively. As the optimum interlayer spacing correlates with the maximum negative binding energy, it signifies stable electronic features. 68,69 The binding energy of a system renders information on the system's stability in that a higher negative value of the binding energy signifies the structure is more stable. For the BeO bilayer system, a negative binding energy is obtained for interlayer spacings ranging from 3.03 to 2.63 Å. In order to apply vertical compression sliding of the upper BeO layer and achieve greater energy corrugation, this range of interlayer spacing is then taken into consideration as a basis to

evaluate the spacing distance that results in a stable (exothermic) structure.

The influence of the transverse xy sliding of the upper BeO layer with respect to the lower BeO layer is studied for two distinct interlayer spacings, 3.03 and 2.63 Å. The sliding induces a change in the potential energy and the polarization deviation at the surface. Figure 2a,b shows the PES and the PDS plots of the BeO system at these two interlayer spacings. The PES and the PDS plots exhibit a periodic pattern, which is consistent with the hexagonal honeycomb geometry of the layered BeO. The structures with the maximal and minimal

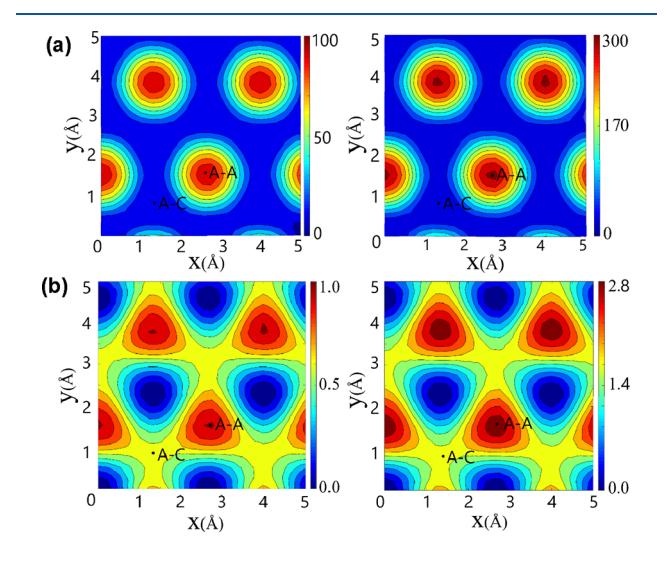


Figure 2. (a) Calculated PES measured in meV and (b) PDS measured in pC/m due to in-plane sliding of the BeO bilayer. The figures on the left and right pertain to interlayer distances of 3.03 and 2.63 Å, respectively. The black dot is used to indicate the location of A–A and A–C stackings resulting from sliding.

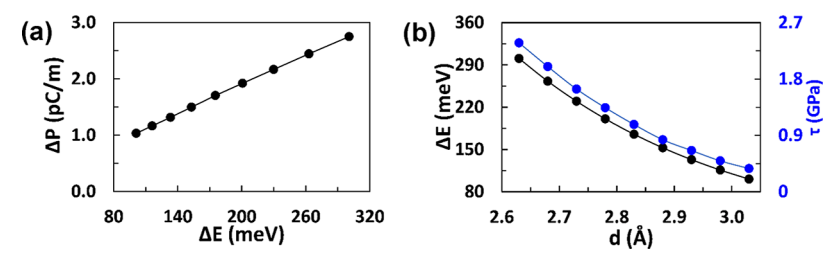


Figure 3. (a) Plotting the maximum deviation of polarization (pC/m) against the corresponding maximum sliding energy barriers (meV). (b) Variation of the interlayer spacing in the BeO bilayer versus deviation of the interlayer shear strength (blue line with filled blue circles) and maximum sliding energy barriers (black line with black circles).

potential energy are identified using the PES. During the xy sliding, the bilayer system demonstrates the maximum potential energy (300 meV for interlayer distance 2.63Å) when it is translated to the A-A configuration (Figure 1c). In contrast, the potential energy is minimal when the bilayer system is translated to the A-B and A-C stacking configurations. Because the potential energies of the A-B and A-C configurations are very similar, it is unclear which structure should be used as the starting point. Therefore, we also calculated the PDS to verify the configuration taken as the initial position. As Figure 2b suggests, the vertical polarization is highest (1.0 pC/m) when the bilayer system resembles the A-A configuration. In addition, polarization is enhanced considerably (2.80 pC/m) when the system is compressed to a lower interlayer distance (2.63 Å). In contrast to the A-A and A-C configurations, the A-B configuration exhibits a relatively small polarization. Therefore, the A-B stacking configuration will be the initial position for further study, and the A–A pattern will be the end point. It is noted that the A–A configuration is not energetically favorable if no mechanical restriction or stimulus is applied to the system. Only a horizontal driving force greater than the resistive force and interlayer shear strength can cause the A-B configuration to transition to the A–A pattern during in-plane xy sliding.

As translating to the A-A geometry while a constant interlayer spacing is maintained improves the vertical polarization substantially, the interlayer sliding and the associated sliding resistance can be viewed as a tribological phenomenon. Thus, the in-plane inlayer sliding that causes the enhancement of the out-of-plane vertical polarization is considered as a tribopiezoelectric event. The tribological energy conversion results in piezoelectricity, which exceeds the sliding resistance energy barrier. For the BeO bilayer system to be translated into the A-A stacking configuration, it is necessary to apply an external translational force as well as pressure, and the tribological energy is thus transformed into electrical energy. As the interlayer spacing is kept fixed, the triboelectric effect is maintained by means of conquering the interlayer sliding energy barrier induced by the resistance and shear strength. Therefore, the tribo-piezoelectric effect is responsible for the out-of-plane vertical polarization prompted by the lateral sliding of the bilayer system.

Cai and co-workers also reported this type of tribopiezoelectric phenomenon in bilayer systems comprising Janus transition metal dichalcogenides. InN and XN (X = B, Al, Ga) structures are also reported to show a similar tribopiezoelectric effect. However, in contrast to the earlier analyses in which the triboelectric effect generated static charges, in this analysis, piezoelectricity was generated by the tribological energy. The energy corrugation (ΔE) in the PES

plot is therefore dependent on the vertical friction of resistance between the layers and an increase in the interlayer friction and resistance will result in a greater corrugation of the energy.⁷¹ The variation trend of the highest polarization deviation (ΔP_{max}) with respect to the highest energy corrugation (ΔE_{max}) is shown in Figure 3. Obviously, ΔP_{max} increases linearly with the rise of $\Delta E_{\rm max}$. The degree of vertical polarization achieved is directly proportional to the amount of energy needed to overcome interlayer resistance. Using eq 4, one can calculate the relative shear strength based on the highest static resistance force due to the lateral sliding process. The shear strength and interlayer separation of the BeO bilayer structure are correlated, as illustrated in Figure 3 (right column). Throughout the vertical compression, we obtained maximum energy corrugation in the range 101-301 meV and a shear strength ranging from 0.4-2.38 GPa for the BeO bilayer system. The values are rather similar to those obtained by Cai et al. for Janus transition metal dichalcogenide.²¹ However, the BeO bilayer system has a greater value of polarization (1-2.69 pC/m) compared to the bilayers of the Janus TMDs and also greater than that of h-BN (0.6–2.3 pC/ m and 2.1 pC/m, respectively). Moreover, the h-BN nanogenerators are reported to show a relatively low ΔE_{max} (210 meV) in contrast to that of the layered BeO system. In addition, an exponential growth in shear strength and maximum energy corrugation is noticed with the decrease in layer spacing. Hence, vertical compression sliding is an excellent method for enhancing the efficiency of the triboelectric to electrical energy conversion.

Nonetheless, through the vertical compressive sliding, a modification in the bilayer structure can be observed, which is attributable to the in-plane strain produced by the vertical stress. When the spacing between the BeO layers is reduced, changes occur in the interaction within the bilayer atoms; the more the interlayer spacing is decreased from the equilibrium position, the stronger the effect develops. The BeO bilayer has a lattice constant of 2.66 Å at the equilibrium interlayer spacing (3.03 Å). However, when the interlayer distance is reduced to 2.73 and 2.63 Å, the lattice constant becomes 2.45 and 2.39Å, respectively. Structural optimization is performed each time the vertical stress is incorporated into the bilayer system, and the altered lattice parameters are taken into consideration for further computations.

In order to study how the charges contribute to the tribopiezoelectric features observed in the BeO bilayer, we calculated the charge density difference of the bilayer system using the relation below,

$$\Delta \Upsilon = \Upsilon_{\text{Bilayer}} - \Upsilon_{\text{Upper}} - \Upsilon_{\text{Lower}}$$
(5)

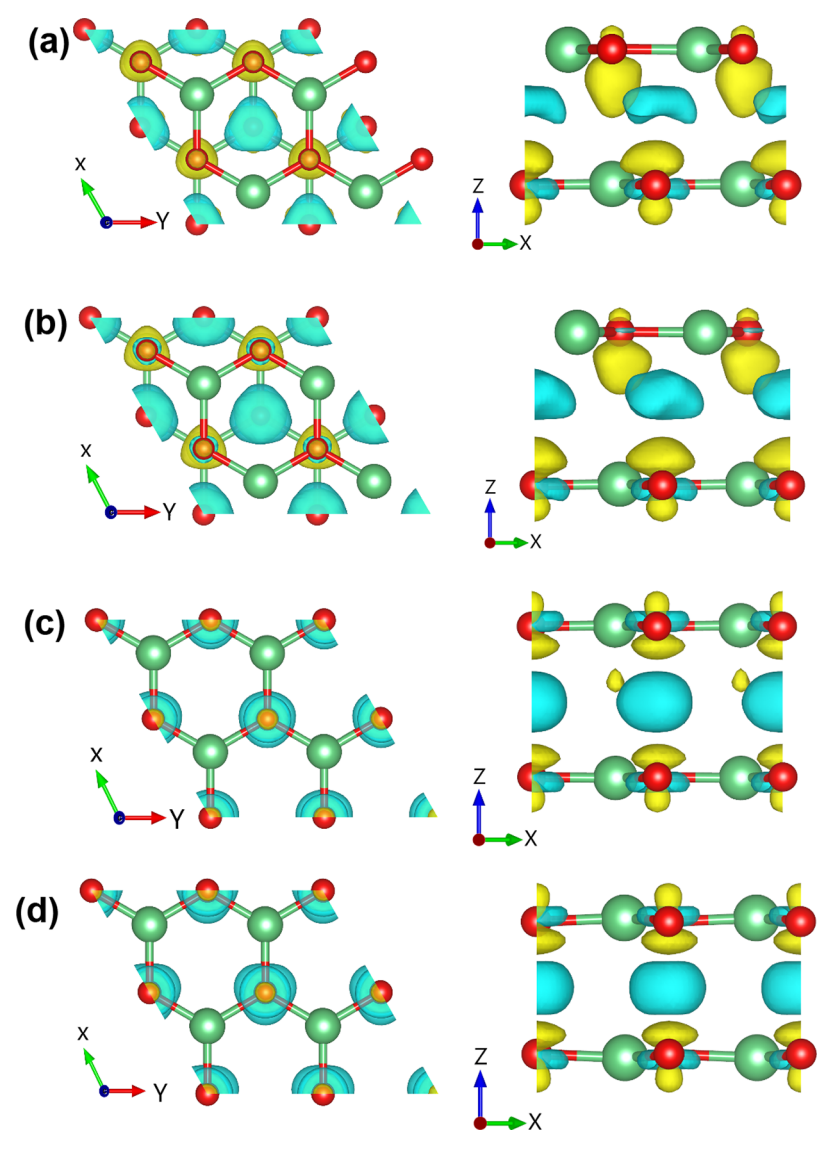


Figure 4. Visualizing the ob86-vdW weighted charge density differences in BeO bilayers. The figures display both top and side views of various stacking patterns. The top row illustrates the A–B configuration with interlayer spacings of (a) 3.03 and (b) 2.63 Å. The bottom row showcases the A–A configuration with interlayer spacings of (c) 3.03 and (d) 2.63 Å. Green spheres denote Be atoms, and red spheres denote O atoms. Charge accumulation is depicted in yellow, while charge depletion is shown in cyan.

Here, $\Upsilon_{\text{Bilaver}}$ stands for the total charge density of the BeO bilayer, Υ_{Upper} refers to the charge density of the upper layer, while Υ_{Lower} symbolizes the charge density of the lower BeO layer. Figure 4 illustrates the charge density difference of the A-A and A-B stacking configurations for the two different interlayer spacings, 3.03 and 2.63 Å. It can be seen that the charge increases near the oxygen atoms of the upper and lower layers as well as at the bilayer interface for both of the interlayer distances (Figure 4). Furthermore, translating the A-B stacking configuration to the A-A pattern results in a drastic escalation in the magnitude of charge near the oxygen atoms. The charge density difference of the A-A configuration is enhanced substantially when the interlayer spacing is decreased from 3.03 to 2.63 Å. The increase of charge near the oxygen atoms of the bilayer implies a greater out-of-plane polarization for the A-A configuration. The alteration of interlayer distance leads to variations in the average charge density difference between the top and bottom layers. Therefore, we calculated the average charge density differences

between the top and the bottom layers of the BeO bilayer. The initial application of this method involves applying zero normal force ($F_{\rm n}=0$) along the z-axis. The charge density difference of the upper layer and the lower layer (symbolized as $\Delta \Upsilon_{\rm Upper}$ and $\Delta \Upsilon_{\rm Lower}$, respectively) are quantified using the relations:

$$\Delta \Upsilon_{\text{Upper}} = \Upsilon_{\text{Upper}}^{\text{O}} - \Upsilon_{\text{Upper}(F_n=0)}^{\text{O}}$$
 (6)

and

$$\Delta \Upsilon_{\text{Lower}} = \Upsilon_{\text{Lower}}^{\text{O}} - \Upsilon_{\text{Lower}(F_n=0)}^{\text{O}}$$
(7)

Here, $\Upsilon^{\rm O}_{\rm Upper}$ and $\Upsilon^{\rm O}_{\rm Lower}$ stand for the average charge densities of the oxygen atoms in the upper and lower monolayers, respectively along the z-axis, while $\Upsilon^{\rm O}_{\rm Upper(F_n=0)}$ and $\Upsilon^{\rm O}_{\rm Lower(F_n=0)}$ are the average density of charges for the upper and lower layers with zero normal force, respectively. The change of the average charge density difference of the upper and lower layer as a function of interlayer spacing ranging from 3.03 to 2.63 Å is illustrated in Figure 5a,b. One can clearly observe that

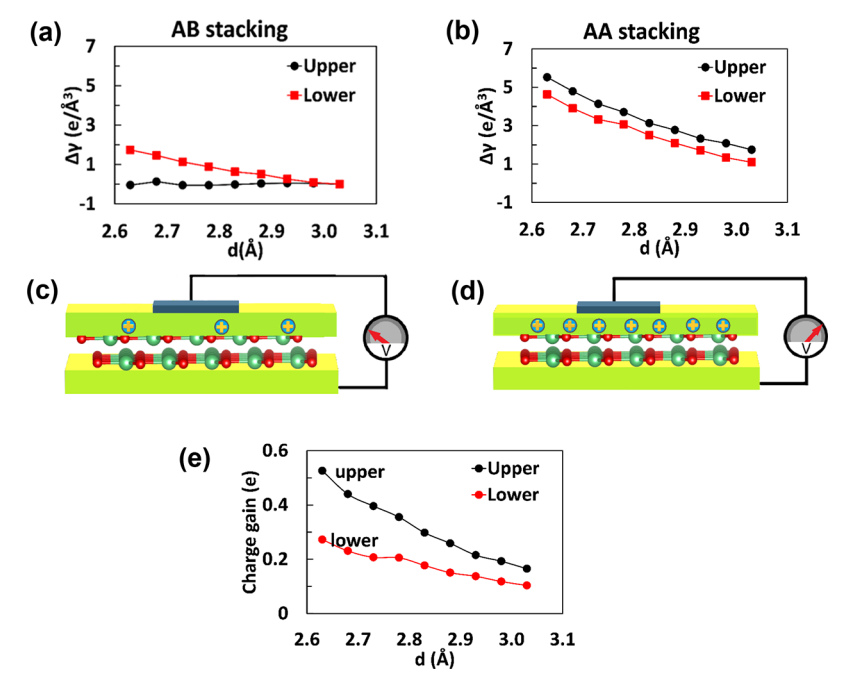


Figure 5. (a, b) Average charge density differences in the BeO bilayer (at scale of 0.001 e/Å^3) of the upper and lower monolayers for the (a) A–B pattern and the (b) A–A pattern versus the variation in the interlayer spacing. The electrodes connected with the surface of the upper and lower layers of the (c) A–B and (d) A–A configurations accumulate relative induced charge and voltage. (e) Gain in charge due to sliding of the two monolayers of the BeO bilayer.

reducing the interlayer separation results in an increased average density of charges on the two monolayers. The magnitude of the charge density is greater for the lower layer compared to the upper layer for the A–B configuration during the application of vertical compression to the bilayer system. However, the dominant contribution of the density of the charge comes from the upper layer in the A–A configuration. The redistribution of the charges in the top and bottom layers of the BeO bilayer is in line with the result of the charge density difference of the bilayer shown in Figure 4.

Vertical compression of the A–B stacking of the BeO bilayer leads to the migration of a reasonable number of electrons to the O atoms. When the upper and lower surfaces are connected to electrodes, a small amount of voltage (along with small inducive charges) will be engendered, as shown in Figure 5c. Translation of the bilayer to the A-A stacking configuration while maintaining the same interlayer spacing results in a greater number of electrons being concentrated near the oxygen atoms. Subsequently, there will be higher induced charges on the top electrode, and the magnitude of the voltage developed between the upper and lower electrodes will be greater, as shown in Figure 5d. Such compressionsliding action in the bilayer system offers a potential way for converting mechanical energy to electricity. Additionally, Figure 5e demonstrates the charge gained at the upper and lower layers when the upper layer is vertically slid. The charge gain (e) is estimated by detracting the charge for the corresponding monolayers of the A-A and A-B stacking arrangements.

In order to enumerate the magnitude of the maximum voltage generated for the A–A stacking, the difference of the electrostatic potential between the oxygen atoms of the upper and lower layers is quantified. The variation of the electrostatic potential difference (ΔU) while changing the interlayer spacing is calculated through the expression:

$$\Delta U = \Delta U_{\text{Upper}} - \Delta U_{\text{Lower}} \tag{8}$$

With

$$\Delta U_{\text{Upper}} = U_{\text{Upper}}^{\text{O}} - U_{\text{Upper}(F_n=0)}^{\text{O}}$$
(9)

and

$$\Delta U_{\text{Lower}} = U_{\text{Lower}}^{\text{O}} - U_{\text{Lower}(F_{\text{h}}=0)}^{\text{O}}$$
(10)

where $U^{\rm O}_{\rm Upper}$ and $U^{\rm O}_{\rm Lower}$ refer to the average electrostatic potential of the oxygen atom of the upper layer and lower layer, respectively. $U^{\rm O}_{\rm Upper(F_n=0)}$ and $U^{\rm O}_{\rm Lower(F_n=0)}$ stand for the average electrostatic potential of the oxygen atom of the upper layer and the lower layer, respectively, with the normal force being zero (0). As Figure 6 suggests, with the decrease of the interlayer spacing, vertical polarization and potential difference between the upper and lower layers increase substantially. During the compression scheme of the A–A configuration, we achieved a generated voltage ranging from 0.15 to 0.22 V by

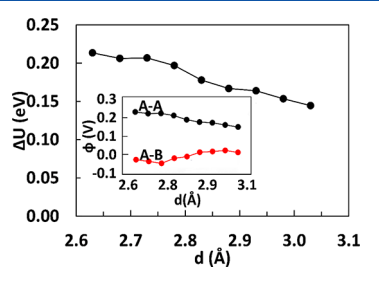


Figure 6. Change of the electrostatic potential differences between the upper- and lower-layer's O atoms for the AA configuration. The inset expresses the evaluation of the generated electric voltages between A–B and A–A configurations when compressing the interlayer spacing of the BeO bilayer from 3.03 to 2.63 Å.

the relation $\phi = \frac{\Delta U}{e}$, where ϕ is the amount of voltage induced and e is the unit charge. Large surfaces may store more charge and provide an enhanced terminal voltage, which affects the peak-induced voltage. When compared to theoretically calculated data, the highest power density and induced output voltage acquired by the experiment often show less than 20% difference. 72,73

Finally, a compression-sliding motion nanoenergy harvesting device is demonstrated to use the BeO bilayer as a nanogenerator. The prototype of the anticipated nanogenerator is shown in Figure 7. For the experimental

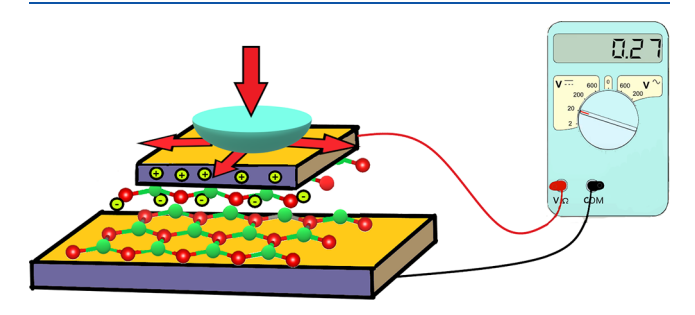


Figure 7. Prototype of BeO bilayer-based sliding and compression nanogenerator. A bilayer of BeO is sandwiched between two electrodes, with the probe placing above the top electrode.

development of the suggested nanogenerator, we utilize the nanoscale probing scheme $^{74-76}$ with a view to encompass force or rotation on a sheet, or a small number of layers of material orientated in a particular direction. Herein, a smaller BeO sheet slides on a comparatively larger BeO monolayer, in accordance with the perpendicular and transversal movement applied through the probing tip. Two edges of the BeO bilayer structure are connected to two electrodes, while the movement of the flake is regulated by a probe connected to the upper electrode. The probe is designed to act as a conductor that connects to the lower electrode.⁷⁷ The most common gold (Au) electrode could be used in the present prototype. Moreover, recent Au/TMD research has demonstrated comparable electrical properties, confirming that the Au electrode has no significant influence on the TMD layer.^{8,78} In addition, as our further analysis reveals, the gold electrode shows minimal effect on the tribo-piezoelectric properties of the BeO bilayers, and adhesion of the gold electrode to the layered BeO surface has greater strength than the adhesion between the two BeO layers. Similar to a conventional electrical system, a voltage drop occurs in the real world due to factors such as wire resistance, load resistance, and the junction at the probe tips. Furthermore, in practical applications of tailoring electrical voltage through vertical sliding cycles of the probe tips, slight variations in the output results can be attributed to pressure fluctuations. The influence of utilizing a Au electrode is examined by considering a relaxed Ausupported BeO monolayer, as depicted in Figure 7.

To achieve a matching lattice parameter with the Au substrate, the lattice parameter of BeO is under a compressive strain of 4.2%. The resulting optimized interlayer spacing between Au and the BeO layer is determined to be 2.54 Å, indicating physical adsorption at the Au-BeO interface. The binding energies per atom for the Au/BeO and BeO bilayers were computed to be -0.604 and -0.0375 eV, respectively. A substantially larger adsorption force exists between the Au

electrode and the BeO contact than exists between two BeO monolayers. A similar outcome was observed in the contact between Au and Janus TMD structure. 21 Figure 8 displays the

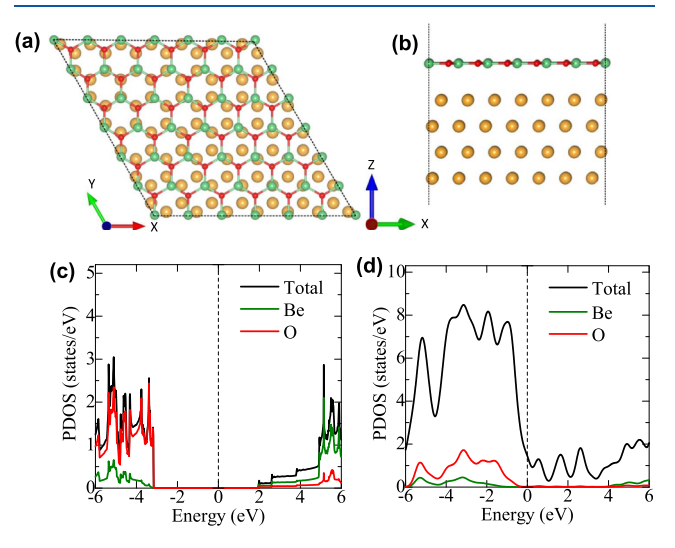


Figure 8. (a) Top view and (b) side view of the gold (Au)/BeO heterostructure. (c) Partial density of states (PDOS) of the BeO bilayer and (d) PDOS for the Au-BeO heterostructure.

atom partial density of states for the Be and O atoms in both the BeO monolayer and the Au/BeO interface. At the interface of Au/BeO, the Fermi level of monolayer BeO is observed to be pinned toward the conduction band, which suggests the presence of an n-type contact. The formation of an interlayer Schottky barrier in the Au-BeO contact results in increased contact resistance, thereby restricting the transfer of charge carriers across the two interfaces. Previous theoretical studies on the contacts between metals and 2D materials corroborate our findings. As per the tribo-piezoelectricity mechanism illustrated in Figure 5, the contact between the electrode and the BeO layer results in the generation of inductive charges, while no transfer of charge occurs from the BeO to the electrode. The presence of a Schottky barrier at the interface between the metal electrode and the BeO layer is expected to impede the flow of charges.

Hence, it can be inferred that the impact of the metal contact on the tribo-piezoelectricity of the BeO bilayer is insignificant. Moreover, recent studies on Au/TMD have demonstrated analogous electrical properties, suggesting that the TMD layer is marginally influenced by the Au electrode. 8,78

The aforementioned findings imply that the tribo-piezoelectric behavior of the BeO bilayer is negligibly impacted by the Au contact, and the compression-sliding scheme is consistent and reliable when used with the BeO bilayer. The interlayer resistive and sliding forces enable the conversion of mechanical energy to electrical energy. The tribological energy therefore contributes to a large portion of the generation of the electrical energy. The amount of electrical energy generated can be estimated by:

$$E_{\rm Elctr} = E_{\rm Tblgcl} \approx Pt$$
 (11)

where $E_{\rm Elctr}$ is the electrical energy produced, $E_{\rm Tblgcl}$ stands for the tribological energy, and P is the quantity of the electrical power produced by the nanogenerator at a particular time t. The setup of Figure 7 can also be studied as a spring-force modeling because the sliding force is applied to the template in a defined direction. The following relations can be used to attain the triboelectric energy and the electrical power produced in each translation cycle:

$$E_{\text{Tblgcl}} = \frac{X\Pi\Delta E_{\text{max}}}{2a} \tag{12}$$

$$P \approx \frac{E_{\text{Tblgcl}}}{t} = \frac{X\Pi\Delta E_{\text{max}}}{2at} \tag{13}$$

Here, the displacement of the probe in each translation cycle is represented by *X*, while *a* is the lattice constant of the bilayer. The quantity of the power delivered by the BeO nanogenerator is therefore determined by the probe's sliding speed (X/t) as well as the maximum energy corrugation (ΔE_{max}), i.e., maximal height of the sliding force barrier. Once pressure is applied vertically to the bilayer prototype through the probe, it leads to a decrease in the interlayer separation, and a higher amount of power is produced. In effect, 1 to 100 nm s⁻¹²¹ of sliding speed can be achieved with the probe tips. If all of the tribological energy is transformed into electrical energy, the tribopiezoelectric property will produce power with the density ranging from 299.6992 to 29969.92 μ W/cm² in each sliding cycle, for a sliding speed of 1–100 nm s⁻¹ when the interlayer separation is lowered to the value of 2.63 Å. Based on experimental findings, a tribo-piezoelectric nanogenerator is capable of providing 7 μ W/cm² power density.⁵⁸ Earlier analyses reported that the power density provided with the piezoelectric¹ nanogenerators is between 4.41 to 5.92 μ W/cm², while for the triboelectric⁷⁹ nanogenerators, the range of power density output is 400 to 50,000 μ W/cm². In contrast to prior theoretical and experimental studies on nanogenerators consisting of graphene oxide and bilayer PVDF-TrFE, monolayer MoS₂ flake, so h-BN polypropylene, GaN nanowire ⁸¹ array and Janus transition metal dichalcogenide, ²¹ and 2D group-III Nitrides, ⁵² our proposed BeO bilayer provides ample maximal power output, as well as a significant amount of induced electrical output voltage (as summarized in Table 1).

In addition, we also broadened our study to a larger BeO bilayer system consisting of a (3×3) bilayer supercell, which yielded a power density output ranging from 299.7571 to 29975.71 μ W/cm². This value is a little higher than the result

Table 1. Comparing the Maximum Power Density and Induced Output Voltage Achieved through the Tribo-Piezoelectric Effect of the Anticipated Configurations with Those Obtained from Previously Studied Configurations

| | tribo-piezoelectric maximum power density (mW cm ⁻²) | | maximum induced output voltage (V) | |
|---|--|------------------------------|------------------------------------|--------------|
| proposed material | theoretical | experimental | theoretical | experimental |
| proposed 2D BeO | ~30 | | 0.22 | |
| bilayer of 2D <i>h</i> -BN ⁵² | ~25 | | 0.172 | |
| bilayer of 2D InN ⁷⁰ | ~74 | | 0.20 | |
| GaN nanowire array ⁸¹ | | | | 0.15-0.35 |
| Janus TMD bilayers ²¹ | ~29.64 | | 0.25 | |
| monolayer MoS ₂ flake ⁸⁰ | | $\sim 2 \times 10^{-4}$ | 0.01825 | 0.015 |
| <i>h</i> -BN polypropylene ¹⁴ | | \sim 29 × 10 ⁻⁴ | | 2.3 |

attained for the BeO unit cell. Besides, the supercell yielded 0.225 V induced voltage and 2.69 pC/m polarization. The supercell structure results in an increase in the surface area, which then causes an upsurge in charge deviation and leads to a rise in power density as well as the amount of voltage induced. Given that there is an electro-mechanical setup (probe pressure and output wire), it is also important to take the calculation's inaccuracy of the generated electrical voltage into consideration. 82-84 In terms of energy harvesting applications, the suggested BeO nanogenerators are promising contenders, specifically for low-power devices and self-driven sensors. Of late, the synthesis of BeO has undergone substantial research and advancement. Zhang et al. 85 reported that the large-scale epitaxial growth of the BeO monolayer on Ag (111) thin films and nanoelectronic and spintronic device applications based on 2D BeO have experienced substantial progress.⁵⁶ It is therefore expected that the experimental realization of BeO bilayer-based tribo-piezoelectric nanogenerators will become viable in the future. Although BeObased energy harvesting technologies are expected to have promising implications in diverse areas, the environmental impact and sustainability aspects of using such energy harvesting devices, especially in applications such as wearable devices, should be better understood. A comprehensive analysis of the entire life cycle of BeO-based devices, from raw material extraction to manufacturing, use, and disposal, should be explored.

CONCLUSIONS

In conclusion, the 2D BeO bilayer is thoroughly inspected to validate the tribo-piezoelectric effect by using ab initio DFT calculations. For lateral sliding, the BeO bilayer demonstrates maximum potential energy (300 meV) with the A-A stacking geometry rather than the A-B and A-C stacking structures. Vertical polarization is the highest (2.69 pC/m) also when the bilayer systems resemble the A-A configuration. For a constant interlayer distance, vertical polarization increased substantially for A-A stacking. Therefore, the tribo-piezoelectric effect is responsible for the out-of-plane vertical polarization induced by the lateral sliding of the bilayer system. The amount of tribological energy was estimated by the degree of shear strength and sliding resistive force. During vertical compressive sliding, the BeO bilayer generates a voltage of \sim 0.22 V. By broadening the BeO bilayer system into a (3 × 3) bilayer supercell, it has been found that power density output significantly improves and ranges from 299.7571 to 29975.71 $\mu W/cm^2$. All of these findings strongly suggest that the BeO bilayers could be used to design a stable, sophisticated, and tremendously efficient nanogenerator for translating and harvesting energy at the nanoscale.

ASSOCIATED CONTENT

Data Availability Statement

The data sets used and/or analyzed during the current study available from the corresponding author on reasonable request.

AUTHOR INFORMATION

Corresponding Author

Md. Sherajul Islam — Department of Electrical & Electronic Engineering, Khulna University of Engineering and Technology, Khulna 9203, Bangladesh; Department of Electrical & Biomedical Engineering, University of Nevada, Reno, Nevada 89557, United States; oorcid.org/0000-0002-6717-2523; Email: sheraj kuet@eee.kuet.ac.bd

Authors

- Md. Yasir Zamil Department of Electrical & Biomedical Engineering, University of Nevada, Reno, Nevada 89557, United States
- Naim Ferdous Department of Electrical & Biomedical Engineering, University of Nevada, Reno, Nevada 89557, United States
- Catherine Stampfl School of Physics, The University of Sydney, Sydney, New South Wales 2006, Australia
- Jeongwon Park Department of Electrical & Biomedical Engineering, University of Nevada, Reno, Nevada 89557, United States; School of Electrical Engineering and Computer Science, University of Ottawa, Ottawa, ON K1N6N5, Canada

Complete contact information is available at: https://pubs.acs.org/10.1021/acsaelm.3c01404

Author Contributions

M.S.I.: conceptualization, methodology, and software. M.Y.Z.: data curation, investigation, and writing—original draft preparation. N.F.: visualization and writing—original draft preparation. C.S.: writing—reviewing and editing. J.P.: supervision and writing—reviewing and editing.

Notes

The authors declare no competing financial interest.

ACKNOWLEDGMENTS

The authors acknowledge support from the National Science Foundation (NSF Convergence Accelerator 1978) under Grant 2235978 and the Bean Space Foundation.

REFERENCES

- (1) Bhavanasi, V.; Kumar, V.; Parida, K.; Wang, J.; Lee, P. S. Enhanced Piezoelectric Energy Harvesting Performance of Flexible PVDF-TrFE Bilayer Films with Graphene Oxide. *ACS Appl. Mater. Interfaces* **2016**, 8 (1), 521–529, DOI: 10.1021/acsami.5b09502.
- (2) Guo, Y.; Zhu, H.; Wang, Q. Piezoelectric Effects in Surface-Engineered Two-Dimensional Group III Nitrides. ACS Appl. Mater. Interfaces 2019, 11 (1), 1033–1039, DOI: 10.1021/acsami.8b17341.
- (3) Patel, A.; Singh, D.; Sonvane, Y.; Thakor, P. B.; Ahuja, R. High Thermoelectric Performance in Two-Dimensional Janus Monolayer Material WS-X (X = Se and Te). ACS Appl Mater Interfaces 2020, 12 (41), 46212–46219.
- (4) Dong, L.; Lou, J.; Shenoy, V. B. Large In-Plane and Vertical Piezoelectricity in Janus Transition Metal Dichalchogenides. *ACS Nano* **2017**, *11* (8), 8242–8248.
- (5) Li, Z. Q.; Zhu, G. L.; Mo, R. J.; Wu, M. Y.; Ding, X. L.; Huang, L. Q.; Wu, Z. Q.; Xia, X. H. Janus Metal-Organic Framework Membranes Boosting the Osmotic Energy Harvesting. *ACS Appl. Mater. Interfaces* **2023**, *15* (19), 23922–23930, DOI: 10.1021/acsami.3c01936.
- (6) Harnden, R.; Carlstedt, D.; Zenkert, D.; Lindbergh, G. Multifunctional Carbon Fiber Composites: A Structural, Energy Harvesting, Strain-Sensing Material. ACS Appl Mater Interfaces 2022, 14 (29), 33871–33880.
- (7) Chang, C.; Tran, V. H.; Wang, J.; Fuh, Y. K.; Lin, L. Direct-Write Piezoelectric Polymeric Nanogenerator with High Energy Conversion Efficiency. *Nano Lett* **2010**, *10* (2), 726–731.
- (8) Lee, J. H.; Park, J. Y.; Cho, E. B.; Kim, T. Y.; Han, S. A.; Kim, T. H.; Liu, Y.; Kim, S. K.; Roh, C. J.; Yoon, H. J.; Ryu, H.; Seung, W.; Lee, J. S.; Lee, J.; Kim, S. W. Reliable Piezoelectricity in Bilayer WSe2

- for Piezoelectric Nanogenerators. Adv. Mater. 2017, 29 (29), 1606667.
- (9) Ballato, A. Dynamic Admittance Matrix of Piezoelectric Cantilever Bimorphs. J. Microelectromech. Syst. 1994, 3 (3), 105–112.
- (10) Mortet, V.; Petersen, R.; Haenen, K.; D'Olieslaeger, M. Wide Range Pressure Sensor Based on a Piezoelectric Bimorph Microcantilever. *Appl. Phys. Lett.* **2006**, *88* (13), 133511.
- (11) Wang, S.; Lin, L.; Wang, Z. L.; Wang, S.; Lin, L.; Wang, Z. L. Nanoscale Triboelectric-Effect-Enabled Energy Conversion for Sustainably Powering Portable Electronics. *Nano Lett.* **2012**, *12* (12), 6339–6346.
- (12) Chen, A.; Zhang, C.; Zhu, G.; Wang, Z. L. Polymer Materials for High-Performance Triboelectric Nanogenerators. *Advanced. Science* **2020**, 7 (14), 2000186.
- (13) Wang, Z. L. Triboelectric Nanogenerator (TENG)—Sparking an Energy and Sensor Revolution. *Adv Energy Mater* **2020**, *10* (17), 2000137.
- (14) Liu, Y.; Ping, J.; Ying, Y. Recent Progress in 2D-Nanomaterial-Based Triboelectric Nanogenerators. *Adv Funct Mater* **2021**, *31* (17), 2009994.
- (15) Zhu, G.; Chen, J.; Liu, Y.; Bai, P.; Zhou, Y. S.; Jing, Q.; Pan, C.; Wang, Z. L. Linear-Grating Triboelectric Generator Based on Sliding Electrification. *Nano Lett* **2013**, *13* (5), 2282–2289.
- (16) Yu, X.; Wang, Z.; Zhao, D.; Ge, J.; Cheng, T.; Wang, Z. L. Triboelectric Nanogenerator with Mechanical Switch and Clamp Circuit for Low Ripple Output. *Nano Res* **2022**, *15*, 2077.
- (17) Wang, S.; Lin, L.; Xie, Y.; Jing, Q.; Niu, S.; Wang, Z. L. Sliding-Triboelectric Nanogenerators Based on in-Plane Charge-Separation Mechanism. *Nano Lett.* **2013**, *13* (5), 2226–2233, DOI: 10.1021/nl400738p.
- (18) Wang, S.; Lin, L.; Xie, Y.; Jing, Q.; Niu, S.; Wang, Z. L. Sliding-Triboelectric Nanogenerators Based on in-Plane Charge-Separation Mechanism. *Nano Lett* **2013**, *13* (5), 2226–2233.
- (19) Cherumannil Karumuthil, S.; Rajeev, S. P.; Varghese, S. Piezo-Tribo Nanoenergy Harvester Using Hybrid Polydimethyl Siloxane Based Nanocomposite. *Nano Energy* **2017**, *40*, 487–494.
- (20) Han, S. A.; Lee, J.; Lin, J.; Kim, S. W.; Kim, J. H. Piezo/Triboelectric Nanogenerators Based on 2-Dimensional Layered Structure Materials. *Nano Energy* **2019**, *57*, 680–691.
- (21) Cai, H.; Guo, Y.; Gao, H.; Guo, W. Tribo-Piezoelectricity in Janus Transition Metal Dichalcogenide Bilayers: A First-Principles Study. *Nano Energy* **2019**, *56*, 33–39.
- (22) Lee, J. S.; Choi, S. H.; Yun, S. J.; Kim, Y. I.; Boandoh, S.; Park, J.-H.; Shin, B. G.; Ko, H.; Lee, S. H.; Kim, Y.-M.; Lee, Y. H.; Kim, K. K.; Kim, S. M. Wafer-Scale Single-Crystal Hexagonal Boron Nitride Film via Self-Collimated Grain Formation. *Science* **2018**, *362* (6416), 817–821.
- (23) Zhao, H.; Xu, M.; Shu, M.; An, J.; Ding, W.; Liu, X.; Wang, S.; Zhao, C.; Yu, H.; Wang, H.; Wang, C.; Fu, X.; Pan, X.; Xie, G.; Wang, Z. L. Underwater Wireless Communication via TENG-Generated Maxwell's Displacement Current. *Nature Communications* **2022**, *13* (1), 1–10.
- (24) Wang, H.; Wang, J.; Yao, K.; Fu, J.; Xia, X.; Zhang, R.; Li, J.; Xu, G.; Wang, L.; Yang, J.; Lai, J.; Dai, Y.; Zhang, Z.; Li, A.; Zhu, Y.; Yu, X.; Wang, Z. L.; Zi, Y. A Paradigm Shift Fully Self-Powered Long-Distance Wireless Sensing Solution Enabled by Discharge-Induced Displacement Current. *Sci. Adv.* **2021**, 7 (39), 6751–6773, DOI: 10.1126/sciadv.abi6751.
- (25) Xiao, X.; Chen, G.; Libanori, A.; Chen, J. Wearable Triboelectric Nanogenerators for Therapeutics. *Trends Chem* **2021**, 3 (4), 279–290.
- (26) Li, Q.; Dai, K.; Zhang, W.; Wang, X.; You, Z.; Zhang, H. Triboelectric Nanogenerator-Based Wearable Electronic Devices and Systems: Toward Informatization and Intelligence. *Digit Signal Process* **2021**, *113*, No. 103038.
- (27) Das, S.; Pandey, D.; Thomas, J.; Roy, T.; Das, S.; Pandey, D.; Thomas, J.; Roy, T. The Role of Graphene and Other 2D Materials in Solar Photovoltaics. *Adv. Mater.* **2019**, *31* (1), 1802722.

- (28) Lee, M. J.; Ahn, J. H.; Sung, J. H.; Heo, H.; Jeon, S. G.; Lee, W.; Song, J. Y.; Hong, K. H.; Choi, B.; Lee, S. H.; Jo, M. H. Thermoelectric Materials by Using Two-Dimensional Materials with Negative Correlation between Electrical and Thermal Conductivity. *Nature Communications* **2016**, *7* (1), 1–7.
- (29) Islam, M. S.; Bhuiyan, A. G.; Tanaka, S.; Makino, T.; Hashimoto, A. Polarized Micro Raman Scattering Spectroscopy for Curved Edges of Epitaxial Graphene. *Appl. Phys. Lett.* **2014**, *105* (24), 243103.
- (30) Islam, M. S.; Sadman, S.; Islam, A. S. M. J.; Park, J. HfO2/TiO2/HfO2 Tri-Layer High-K Gate Oxide Based MoS2 Negative Capacitance FET with Steep Subthreshold Swing. *AIP Adv.* **2020**, *10* (3), No. 035202.
- (31) Islam, M. S.; Ushida, K.; Tanaka, S.; Hashimoto, A. Numerical Experiments on Phonon Properties of Isotope and Vacancy-Type Disordered Graphene. *Diam Relat Mater* **2013**, *40*, 115–122.
- (32) Islam, M. S.; Mazumder, A. A. M.; Sohag, M. U.; Sarkar, M. M. H.; Stampfl, C.; Park, J. Growth Mechanisms of Monolayer Hexagonal Boron Nitride (h -BN) on Metal Surfaces: Theoretical Perspectives. *Nanoscale Adv* **2023**, *5* (16), 4041–4064.
- (33) Islam, M. S.; Mojumder, M. R. H.; Ferdous, N.; Park, J. Germanene/2D-SiC van Der Waals Heterobilayer: Structural Features and Tunable Electronic Properties. *Mater Today Commun* **2021**, *26*, No. 101718.
- (34) Islam, M. S.; Mia, I.; Ahammed, S.; Stampfl, C.; Park, J. Exceptional In-Plane and Interfacial Thermal Transport in Graphene/2D-SiC van Der Waals Heterostructures. *Scientific Reports* **2020**, *10* (1), 1–16.
- (35) Islam, Md. S.; Tamakawa, D.; Tanaka, S.; Makino, T.; Hashimoto, A. Polarized Microscopic Laser Raman Scattering Spectroscopy for Edge Structure of Epitaxial Graphene and Localized Vibrational Mode. *Carbon N Y* **2014**, *77*, 1073–1081.
- (36) Islam, M. S.; Ushida, K.; Tanaka, S.; Makino, T.; Hashimoto, A. Effect of Boron and Nitrogen Doping with Native Point Defects on the Vibrational Properties of Graphene. *Comput. Mater. Sci.* **2014**, *94* (C), 35–43.
- (37) Guan, Z.; Ni, S.; Hu, S. Tuning the Electronic and Magnetic Properties of Graphene Flake Embedded in Boron Nitride Nanoribbons with Transverse Electric Fields: First-Principles Calculations. ACS Omega 2019, 4 (6), 10293–10301, DOI: 10.1021/acsomega.9b00752.
- (38) Hu, A. M.; Wang, L. L.; Xiao, W. Z.; Meng, B. Electronic Structures and Magnetic Properties in Cu-Doped Two-Dimensional Dichalcogenides. *Physica E Low Dimens Syst Nanostruct* **2015**, 73, 69–75
- (39) Li, L.; Han, W.; Pi, L.; Niu, P.; Han, J.; Wang, C.; Su, B.; Li, H.; Xiong, J.; Bando, Y.; Zhai, T. Emerging In-Plane Anisotropic Two-Dimensional Materials. *InfoMat* **2019**, *1* (1), 54–73.
- (40) Atallah, N. I.; El-Kemary, M.; Pascale, F.; El-Kelany, K. E. Extraordinary Piezoelectric Effect Induced in Two-Dimensional Rare Earth Monochalcogenides via Reducing System Dimensionality. *Journal of Materiomics* **2023**, *9* (1), 72–81.
- (41) Sohag, M. U.; Islam, M. S.; Hosen, K.; Fahim, M. A. I.; Sarkar, M. M. H.; Park, J. Dual Source Negative Capacitance GaSb/InGaAsSb/InAs Heterostructure Based Vertical TFET with Steep Subthreshold Swing and High on-off Current Ratio. *Results Phys* **2021**, *29*, No. 104796.
- (42) Mojumder, M. R. H.; Islam, M. S.; Park, J. Germanene/2D-AlP van Der Waals Heterostructure: Tunable Structural and Electronic Properties. *AIP Adv* **2021**, *11* (1), 15126.
- (43) Islam, M. R.; Islam, M. S.; Zamil, M. Y.; Ferdous, N.; Stampfl, C.; Park, J.; Hossain, M. K. Two-Dimensional BAs/GeC van Der Waals Heterostructures: A Widely Tunable Photocatalyst for Water Splitting and Hydrogen Production. *J. Phys. Chem. Solids* **2023**, *176*, No. 111263.
- (44) Liu, Y.; Liu, S.; Li, B.; Yoo, W. J.; Hone, J. Identifying the Transition Order in an Artificial Ferroelectric van Der Waals Heterostructure. *Nano Lett.* **2022**, 22 (3), 1265–1269, DOI: 10.1021/acs.nanolett.1c04467.

- (45) Weston, A.; Castanon, E. G.; Enaldiev, V.; Ferreira, F.; Bhattacharjee, S.; Xu, S.; Corte-León, H.; Wu, Z.; Clark, N.; Summerfield, A.; Hashimoto, T.; Gao, Y.; Wang, W.; Hamer, M.; Read, H.; Fumagalli, L.; Kretinin, A. V.; Haigh, S. J.; Kazakova, O.; Geim, A. K.; Fal'ko, V. I.; Gorbachev, R. Interfacial Ferroelectricity in Marginally Twisted 2D Semiconductors. *Nature Nanotechnology* **2022**, *17* (4), 390–395.
- (46) Rogée, L.; Wang, L.; Zhang, Y.; Cai, S.; Wang, P.; Chhowalla, M.; Ji, W.; Lau, S. P. Ferroelectricity in Untwisted Heterobilayers of Transition Metal Dichalcogenides. *Science* **2022**, *376* (6596), 973–978, DOI: 10.1126/science.abm5734.
- (47) Xiao, J.; Wang, Y.; Wang, H.; Pemmaraju, C. D.; Wang, S.; Muscher, P.; Sie, E. J.; Nyby, C. M.; Devereaux, T. P.; Qian, X.; Zhang, X.; Lindenberg, A. M. Berry Curvature Memory through Electrically Driven Stacking Transitions. *Nature Physics* **2020**, *16* (10), 1028–1034.
- (48) Yasuda, K.; Wang, X.; Watanabe, K.; Taniguchi, T.; Jarillo-Herrero, P. Stacking-Engineered Ferroelectricity in Bilayer Boron Nitride. *Science* **1979**, 372 (6549), 1458–1462, DOI: 10.1126/science.abd3230.
- (49) Vizner Stern, M.; Waschitz, Y.; Cao, W.; Nevo, I.; Watanabe, K.; Taniguchi, T.; Sela, E.; Urbakh, M.; Hod, O.; Ben Shalom, M. Interfacial Ferroelectricity by van Der Waals Sliding. *Science* **2021**, 372 (6549), 142–1466, DOI: 10.1126/science.abe8177.
- (50) Yang, Q.; Wu, M.; Li, J. Origin of Two-Dimensional Vertical Ferroelectricity in WTe 2 Bilayer and Multilayer. *J. Phys. Chem. Lett.* **2018**, 9 (24), 7160–7164, DOI: 10.1021/ACS.JPCLETT.8B03654.
- (51) Fei, Z.; Zhao, W.; Palomaki, T. A.; Sun, B.; Miller, M. K.; Zhao, Z.; Yan, J.; Xu, X.; Cobden, D. H. Ferroelectric Switching of a Two-Dimensional Metal. *Nature* **2018**, *560* (7718), 336–339.
- (52) Zamil, M. Y.; Islam, M. S.; Stampfl, C.; Park, J. Tribo-Piezoelectricity in Group III Nitride Bilayers: A Density Functional Theory Investigation. *ACS Appl. Mater. Interfaces* **2022**, *14*, 20856–20865, DOI: 10.1021/ACSAMI.2C00855.
- (53) Chakraborty, B.; Borgohain, M. M.; Adhikary, N. C. Structural and Electronic Properties of Stanene-BeO Heterobilayer. *Mater. Res. Express* **2020**, *7*, No. 015029, DOI: 10.1088/2053-1591/ab6091.
- (54) Xia, C.; Li, W.; Ma, D.; Zhang, L. Electronic and Thermal Properties of Monolayer Beryllium Oxide from First Principles. *Nanotechnology* **2020**, *31* (37), 375705.
- (55) Islam, A. S. M. J.; Islam, Md. S.; Mim, N. Z.; Akbar, Md. S.; Hasan, Md. S.; Islam, Md. R.; Stampfl, C.; Park, J. Vacancy-Induced Thermal Transport and Tensile Mechanical Behavior of Monolayer Honeycomb BeO. ACS Omega 2022, 7 (5), 4525–4537.
- (56) Liu, H.; Feng, K.; Lu, H.; Meng, X. First-Principles Calculations of the BeO Monolayer with Chemical Functionalization. *Phys. Chem. Phys.* **2022**, 24 (13), 7797–7804.
- (57) Alyörük, M. M. Piezoelectric Properties of Monolayer II–VI Group Oxides by First-principles Calculations. *physica status solidi (b)* **2016**, 253 (12), 2534–2539.
- (58) Yang, X.; Daoud, W. A. Triboelectric and Piezoelectric Effects in a Combined Tribo-Piezoelectric Nanogenerator Based on an Interfacial ZnO Nanostructure. *Adv Funct Mater* **2016**, *26* (45), 8194–8201.
- (59) Giannozzi, P.; Baseggio, O.; Bonfâ, P.; Brunato, D.; Car, R.; Carnimeo, I.; Cavazzoni, C.; De Gironcoli, S.; Delugas, P.; Ferrari Ruffino, F.; Ferretti, A.; Marzari, N.; Timrov, I.; Urru, A.; Baroni, S. Quantum ESPRESSO toward the Exascale. *J. Chem. Phys.* **2020**, *152* (15), No. 154105.
- (60) Giannozzi, P.; Baroni, S.; Bonini, N.; Calandra, M.; Car, R.; Cavazzoni, C.; Ceresoli, D.; Chiarotti, G. L.; Cococcioni, M.; Dabo, I.; Dal Corso, A.; De Gironcoli, S.; Fabris, S.; Fratesi, G.; Gebauer, R.; Gerstmann, U.; Gougoussis, C.; Kokalj, A.; Lazzeri, M.; Martin-Samos, L.; Marzari, N.; Mauri, F.; Mazzarello, R.; Paolini, S.; Pasquarello, A.; Paulatto, L.; Sbraccia, C.; Scandolo, S.; Sclauzero, G.; Seitsonen, A. P.; Smogunov, A.; Umari, P.; Wentzcovitch, R. M. QUANTUM ESPRESSO: A Modular and Open-Source Software Project for Quantum of Materials. *Journal of Physics: Condensed Matter* 2009, 21 (39), No. 395502.

- (61) Joubert, D. From Ultrasoft Pseudopotentials to the Projector Augmented-Wave Method. *Phys. Rev. B Condens. Matter Mater. Phys.* **1999**, *59* (3), 1758–1775.
- (62) Perdew, J. P.; Burke, K.; Ernzerhof, M. Generalized Gradient Approximation Made Simple. *Phys. Rev. Lett.* **1996**, 77 (18), 3865–3868.
- (63) Pack, J. D.; Monkhorst, H. J. "special Points for Brillouin-Zone Integrations"-a Reply. *Phys Rev B* **1977**, *16* (4), 1748–1749.
- (64) Klimeš, J.; Bowler, D. R.; Michaelides, A. Chemical Accuracy for the van Der Waals Density Functional. *J. Phys.: Condens. Matter* **2010**, 22 (2), No. 022201.
- (65) Klime, J.; Bowler, D. R.; Michaelides, A. Van Der Waals Density Functionals Applied to Solids. *Phys. Rev. B Condens. Matter Mater. Phys.* **2011**, 83 (19), 195131.
- (66) Yuan, D.; Liao, H.; Hu, W. Assessment of van Der Waals Inclusive Density Functional Theory Methods for Adsorption and Selective Dehydrogenation of Formic Acid on Pt(111) Surface. *Phys. Chem. Chem. Phys.* **2019**, *21* (37), 21049–21056.
- (67) Baima, J.; Erba, A.; Rérat, M.; Orlando, R.; Dovesi, R. Beryllium Oxide Nanotubes and Their Connection to the Flat Monolayer. *J. Phys. Chem. C* **2013**, *117* (24), 12864–12872, DOI: 10.1021/JP402340Z.
- (68) Sarker, J. D.; Islam, M. S.; Ferdous, N.; Sarker, P. P.; Bhuiyan, A. G.; Makino, T.; Hashimoto, A. Tunable Electronic Properties in Bismuthene/2D Silicon Carbide van Der Waals Heterobilayer. *Jpn. J. Appl. Phys.* **2020**, *59*, SCCC03.
- (69) Rashid, A. S.; Islam, M. S.; Ferdous, N.; Anindya, K. N.; Park, J.; Hashimoto, A. Widely Tunable Electronic Properties in Graphene/Two-Dimensional Silicon Carbide van Der Waals Heterostructures. *Journal of Computational Electronics* **2019**, *18* (3), 836–845.
- (70) Islam, M. S.; Zamil, M. Y.; Mojumder, M. R. H.; Stampfl, C.; Park, J. Strong Tribo-Piezoelectric Effect in Bilayer Indium Nitride (InN). *Scientific Reports* **2021**, *11* (1), 1–12.
- (71) Zhang, J.; Bai, Y.; An, L.; Zhang, B.; Zhang, J.; Yu, Y.; Wang, C. M. Reduction of Interlayer Friction between Bilayer Hexagonal Boron Nitride Nanosheets Induced by Electron Redistribution. *J. Appl. Phys.* **2019**, *126* (3), No. 035104.
- (72) Zhu, G.; Yang, R.; Wang, S.; Wang, Z. L. Flexible High-Output Nanogenerator Based on Lateral ZnO Nanowire Array. *Nano Lett* **2010**, *10* (8), 3151–3155.
- (73) He, X.; Guo, H.; Yue, X.; Gao, J.; Xi, Y.; Hu, C. Improving Energy Conversion Efficiency for Triboelectric Nanogenerator with Capacitor Structure by Maximizing Surface Charge Density. *Nanoscale* **2015**, 7 (5), 1896–1903.
- (74) Vu, C. C.; Zhang, S.; Urbakh, M.; Li, Q.; He, Q. C.; Zheng, Q. Observation of Normal-Force-Independent Superlubricity in Mesoscopic Graphite Contacts. *Phys. Rev. B* **2016**, 94 (8), No. 081405.
- (75) Leven, I.; Krepel, D.; Shemesh, O.; Hod, O. Robust Superlubricity in Graphene/h-BN Heterojunctions. *Journal of Physical Chemistry Letters* **2013**, *4* (1), 115–120.
- (76) Sheehan, P. E.; Lieber, C. M. Friction between van Der Waals Solids during Lattice Directed Sliding. *Nano Lett.* **2017**, *17* (7), 4116–4121, DOI: 10.1021/ACS.NANOLETT.7B00871.
- (77) Liu, J.; Goswami, A.; Jiang, K.; Khan, F.; Kim, S.; McGee, R.; Li, Z.; Hu, Z.; Lee, J.; Thundat, T. Direct-Current Triboelectricity Generation by a Sliding Schottky Nanocontact on MoS 2 Multilayers. *Nat Nanotechnol* **2018**, *13* (2), 112–116.
- (78) Brennan, C. J.; Ghosh, R.; Koul, K.; Banerjee, S. K.; Lu, N.; Yu, E. T. Out-of-Plane Electromechanical Response of Monolayer Molybdenum Disulfide Measured by Piezoresponse Force Microscopy. *Nano Lett* **2017**, *17* (9), 5464–5471.
- (79) Wang, S.; Xie, Y.; Niu, S.; Lin, L.; Liu, C.; Zhou, Y. S.; Wang, Z. L. Maximum Surface Charge Density for Triboelectric Nanogenerators Achieved by Ionized-Air Injection: Methodology and Theoretical Understanding. *Adv. Mater.* **2014**, 26 (39), 6720–6728.
- (80) Wu, W.; Wang, L.; Li, Y.; Zhang, F.; Lin, L.; Niu, S.; Chenet, D.; Zhang, X.; Hao, Y.; Heinz, T. F.; Hone, J.; Wang, Z. L. Piezoelectricity of Single-Atomic-Layer MoS2 for Energy Conversion and Piezotronics. *Nature* **2014**, *514* (7253), 470–474.

- (81) Huang, C.; Song, J.; Lee, W. F.; Ding, Y.; Gao, Z.; Hao, Y.; Chen, L. J.; Wang, Z. L. GaN Nanowire Arrays for High-Output Nanogenerators. J. Am. Chem. Soc. 2010, 132 (13), 4766–4771.
- (82) Fan, F. R.; Tang, W.; Wang, Z. L. Flexible Nanogenerators for Energy Harvesting and Self-Powered Electronics. *Adv. Mater.* **2016**, 28 (22), 4283–4305.
- (83) Zhang, H.; Yang, Y.; Su, Y.; Chen, J.; Hu, C.; Wu, Z.; Liu, Y.; Ping Wong, C.; Bando, Y.; Wang, Z. L. Triboelectric Nanogenerator as Self-Powered Active Sensors for Detecting Liquid/Gaseous Water/Ethanol. *Nano Energy* **2013**, 2 (5), 693–701.
- (84) Wang, Z. L.; Wu, W. Nanotechnology-Enabled Energy Harvesting for Self-Powered Micro-/Nanosystems. *Angewandte Chemie International Edition* **2012**, *51* (47), 11700–11721.
- (85) Zhang, H.; Holbrook, M.; Cheng, F.; Nam, H.; Liu, M.; Pan, C. R.; West, D.; Zhang, S.; Chou, M. Y.; Shih, C. K. Epitaxial Growth of Two-Dimensional Insulator Monolayer Honeycomb BeO. *ACS Nano* **2021**, *15* (2), 2497–2505, DOI: 10.1021/ACSNANO.0C06596.